Observations of Ejecta Clouds Produced by Impacts onto Saturn's Rings

Matthew S. Tiscareno *et al.*

Science **340**, 460 (2013);
DOI: 10.1126/science.1233524

Science (print ISSN 0036-8075; online ISSN 1095-9203) is published weekly, except the last week in December, by the American Association for the Advancement of Science, 1200 New York Avenue NW, Washington, DC 20005.

have permitted us to deduce the involvement of unstable, non-isolable intermediates that have previously eluded more conventional mechanistic studies. Similarly innovative studies that delineate reactivity patterns of more capricious but abundant metals (Cu, Fe, Ni) are needed to further understand and develop new catalytic processes, reducing synthetic reliance on well-behaved but rare and expensive transition metals (Pd, Rh, Ru). Moreover, the mechanistic insights presented in this study, specifically the formation of the active cycloaddition complex with two differentiable copper atoms, imply a unified reactivity of electronically rich σ-acetylides (1-halo- or 1-metallo-) with 1,3-dipoles (e.g., azides, nitrile oxides, and nitrones). As such, we propose a common reactivity trend in which any σ-acetylide that can effectively recruit a π-bound copper atom will undergo annulation with a compatible dipolar partner.

References and Notes

1. W. M. Haynes, *CRC Handbook of Chemistry and Physics* (CRC Press, Boca Raton, FL, ed. 93, 2012).
2. A. Moen, D. G. Nicholson, *J. Chem. Soc. Faraday Trans.* **91**, 3529 (1995).
3. H. V. R. Dias, J. A. Flores, J. Wu, P. Kroll, *J. Am. Chem. Soc.* **131**, 11249 (2009).
4. B. J. Hathaway, in *Comprehensive Coordination Chemistry*, G. Wilkinson, Ed. (Pergamon, Oxford, 1987), vol. 5, pp. 533–757.
5. S. V. Ley, A. W. Thomas, *Angew. Chem. Int. Ed.* **42**, 5400 (2003).
6. F. Monnier, M. Taillefer, *Angew. Chem. Int. Ed.* **48**, 6954 (2009).
7. S. Schindler, *Eur. J. Inorg. Chem.* **2000**, 2311 (2000).
8. W. G. Nigh, in *Oxidation in Organic Chemistry*, W. S. Trahanovsky, Ed. (Academic Press, New York, 1973), part B, pp. 1–95.
9. C. W. Tornøe, C. Christensen, M. Meldal, *J. Org. Chem.* **67**, 3057 (2002).
10. V. V. Rostovtsev, L. G. Green, V. V. Fokin, K. B. Sharpless, *Angew. Chem. Int. Ed.* **41**, 2596 (2002).
11. M. Meldal, C. W. Tornøe, *Chem. Rev.* **108**, 2952 (2008).
12. J. E. Hein, V. V. Fokin, *Chem. Soc. Rev.* **39**, 1302 (2010).
13. F. Himo *et al.*, *J. Am. Chem. Soc.* **127**, 210 (2005).
14. V. O. Rodionov, V. V. Fokin, M. G. Finn, *Angew. Chem. Int. Ed.* **44**, 2210 (2005).
15. V. O. Rodionov, S. I. Presolski, D. D. Díaz, V. V. Fokin, M. G. Finn, *J. Am. Chem. Soc.* **129**, 12705 (2007).
16. G.-C. Kuang *et al.*, *J. Am. Chem. Soc.* **133**, 13984 (2011).
17. B. F. Straub, *Chem. Commun.* **2007**, 3868 (2007).
18. M. Ahlquist, V. V. Fokin, *Organometallics* **26**, 4389 (2007).
19. B. H. M. Kuijpers *et al.*, *Synlett* **2005**, 3059 (2005).
20. J. E. Hein, J. C. Tripp, L. B. Krasnova, K. B. Sharpless, V. V. Fokin, *Angew. Chem. Int. Ed.* **48**, 8018 (2009).
21. D. V. Partyka *et al.*, *Organometallics* **28**, 6171 (2009).
22. Y. Zhou, T. Lecourt, L. Micouin, *Angew. Chem. Int. Ed.* **49**, 2607 (2010).
23. C. Nolte, P. Mayer, B. F. Straub, *Angew. Chem. Int. Ed.* **46**, 2101 (2007).
24. D. G. Blackmond, *Angew. Chem. Int. Ed.* **44**, 4302 (2005).
25. Although the starting acetylide complex **2** is stable to atmospheric moisture, acidic or strongly protic solvents or azides can sever the Cu-acetylide bond. The liberated Cu(I) will, in turn, catalyze the formation of triazolide **4**, albeit at a substantially lower rate than that observed by copper catalyst **3**. Therefore, it is best to use nonprotic solvents and azides to observe the highest difference in rate between the catalyzed and noncatalyzed experiments.
26. C. Boehme, G. Frenking, *Organometallics* **17**, 5801 (1998).
27. G. J. Kubas, B. Monzyk, A. L. Crumbliss, *Inorg. Synth.* **19**, 90 (1979).
28. B. M. Mykhalichko, O. N. Temkin, M. G. Mys'kiv, *Russ. Chem. Rev.* **69**, 957 (2000).
29. Although complexation of NHCs to transition metals is strongly governed by σ-donation, recent investigations have shown that π-backbonding can account for as much as 30% of the overall bonding character.
30. M. D. Sanderson, J. W. Kamplain, C. W. Bielawski, *J. Am. Chem. Soc.* **128**, 16514 (2006).
31. A. Comas-Vives, J. N. Harvey, *Eur. J. Inorg. Chem.*, **2011**, 5025 (2011).

Acknowledgments: This work was supported by grants from the NSF (CHE-0848982) and the NIH National Institute of General Medical Sciences (GM-087620). We thank B. Webb for assistance with mass spectrometry analyses, S. W. Kwok (Harvard University) for support with reaction calorimetry, and J. Hein (University of California, Merced) for helpful scientific discussions.

Supplementary Materials

www.sciencemag.org/cgi/content/full/science.1229506/DC1
Supplementary Text
Figs. S1 to S14
Tables S1 to S5
NMR Spectra
References (*32*–*34*)

30 August 2012; accepted 29 January 2013
Published online 4 April 2013;
10.1126/science.1229506

Observations of Ejecta Clouds Produced by Impacts onto Saturn's Rings

Matthew S. Tiscareno,[1]* Colin J. Mitchell,[2] Carl D. Murray,[3] Daiana Di Nino,[2] Matthew M. Hedman,[1] Jürgen Schmidt,[4,5] Joseph A. Burns,[6,7] Jeffrey N. Cuzzi,[8] Carolyn C. Porco,[2] Kevin Beurle,[3] Michael W. Evans[1]

We report observations of dusty clouds in Saturn's rings, which we interpret as resulting from impacts onto the rings that occurred between 1 and 50 hours before the clouds were observed. The largest of these clouds was observed twice; its brightness and cant angle evolved in a manner consistent with this hypothesis. Several arguments suggest that these clouds cannot be due to the primary impact of one solid meteoroid onto the rings, but rather are due to the impact of a compact stream of Saturn-orbiting material derived from previous breakup of a meteoroid. The responsible interplanetary meteoroids were initially between 1 centimeter and several meters in size, and their influx rate is consistent with the sparse prior knowledge of smaller meteoroids in the outer solar system.

Quantifying the mass flux onto Saturn's rings has been a long-desired goal. Mass infall likely dominates the rings' coloration and their levels of non-ice pollution, as well as influencing angular momentum transport and erosion of particles, all of which in turn have the potential to set limits on the age of the rings (*1*–*3*). Impacts may be a trigger mechanism for the "spokes" observed in the B ring (*4*, *5*), and they may be responsible for producing some dust outbursts observed in the F ring (*6*, *7*). Additionally, direct measurement of the mass infall onto Saturn's rings would constrain the population of interplanetary meteoroids in the outer solar system, which is poorly determined for macroscopic particles (*1*, *8*). However, although impact flashes have been observed on Earth's Moon [e.g., (*9*)], efforts to detect impact flashes in the outer solar system have been unsuccessful (*10*, *11*).

Here, we report images of ejecta clouds above Saturn's rings (Fig. 1), obtained by Cassini's Imaging Science Subsystem (*12*, *13*). These features are normally not visible owing to low contrast with the background ring, but there are two particular viewing geometries in which they become visible: (i) during saturnian equinox, at which time the background ring becomes very dark, and (ii) when Cassini views the rings at high resolution and very high phase angle, at which time the dusty features appear very bright (Fig. 2).

The saturnian equinox, which occurs every ~14.5 years and is closely accompanied by edge-on viewing of Saturn's rings from Earth, has led to many scientific discoveries over the centuries since 1612, when the ring system's disappearance from Galileo's view gave the first hint of its disk geometry (*14*). The 2009 equinox was the first for which an observer (namely, the Cassini spacecraft) was in place at close range and high saturnian latitudes. During a few days surrounding the precise moment of the Sun's passage through the ring plane, the main rings provided an unusually dark background, due to the edge-on illumination, while anything (e.g., an ejecta cloud) extending vertically out of the ring plane

[1]Center for Radiophysics and Space Research, Cornell University, Ithaca, NY 14853, USA. [2]CICLOPS, Space Science Institute, Boulder, CO 80301, USA. [3]Astronomy Unit, Queen Mary University of London, London E1 4NS, UK. [4]Department of Physics, Astronomy Division, University of Oulu, FI-90014, Finland. [5]Institute for Physics and Astronomy, University of Potsdam, 14476 Potsdam-Golm, Germany. [6]Department of Astronomy, Cornell University, Ithaca, NY 14853, USA. [7]College of Engineering, Cornell University, Ithaca, NY 14853, USA. [8]NASA Ames Research Center, Moffett Field, CA 94035, USA.

*Corresponding author. E-mail: matthewt@astro.cornell.edu

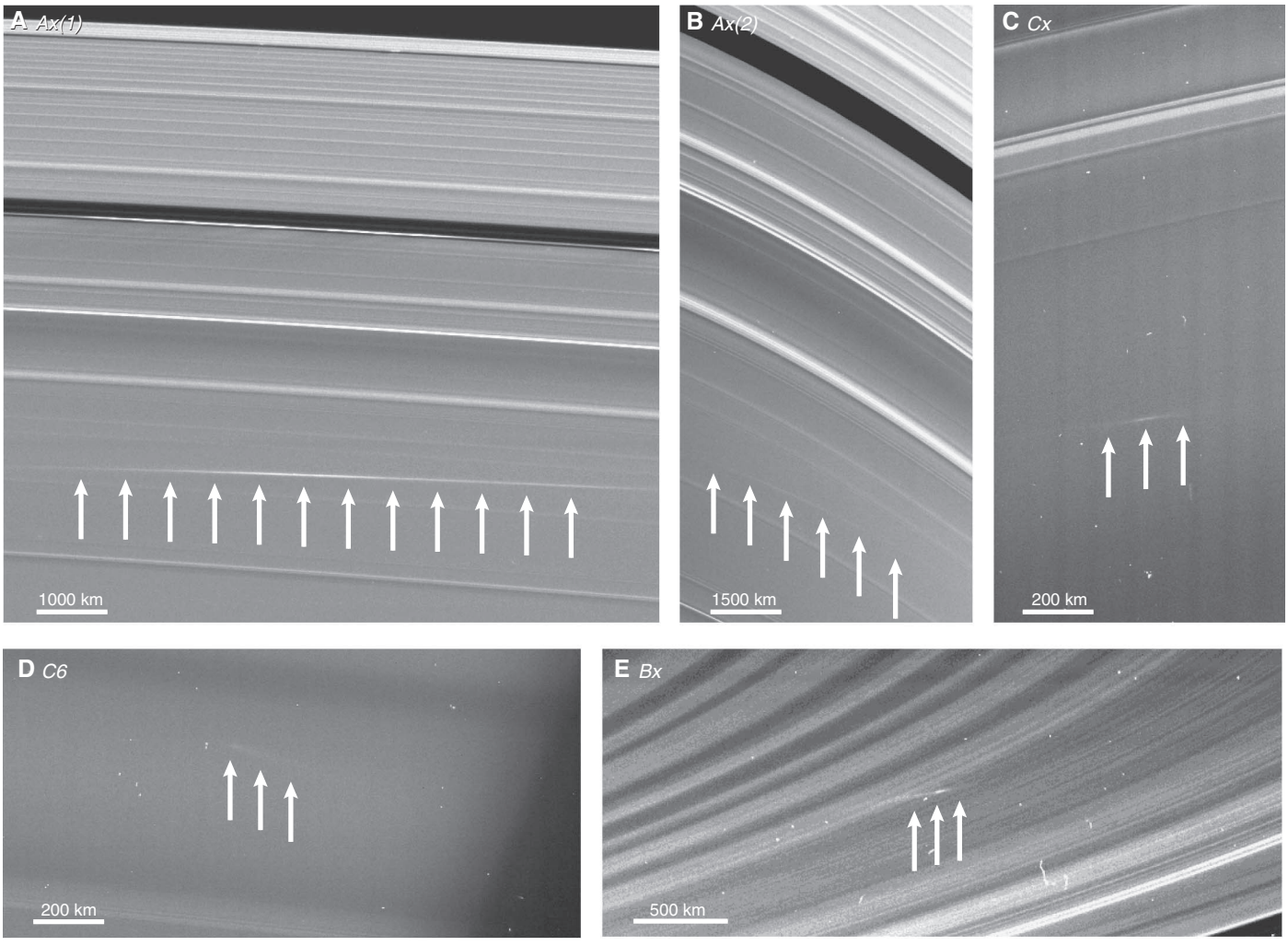

Fig. 1. Ejecta clouds. (**A** and **B**) Two views of one cloud in the A ring, taken 24.5 hours apart [code-named Ax(1) and Ax(2)]; (**C**) a cloud in the C ring (code-named Cx); (**D**) another cloud in the C ring (code-named C6); and (**E**) a cloud in the B ring (code named Bx). Arrows point to the cloud structures, which are visibly canted from the surrounding azimuthally aligned features. The images shown here were all taken during the 2009 saturnian equinox event except (D) (containing C6), which was taken at high resolution and very high phase angle in 2012. The clouds are reprojected onto a radius-longitude grid in Fig. 3A and fig. S2. The features C1 through C5, which were seen in the C ring in 2005 at geometries similar to that for C6 and which are smeared owing to orbital motion of the features during the image exposure, are shown in figs. S1 and S3.

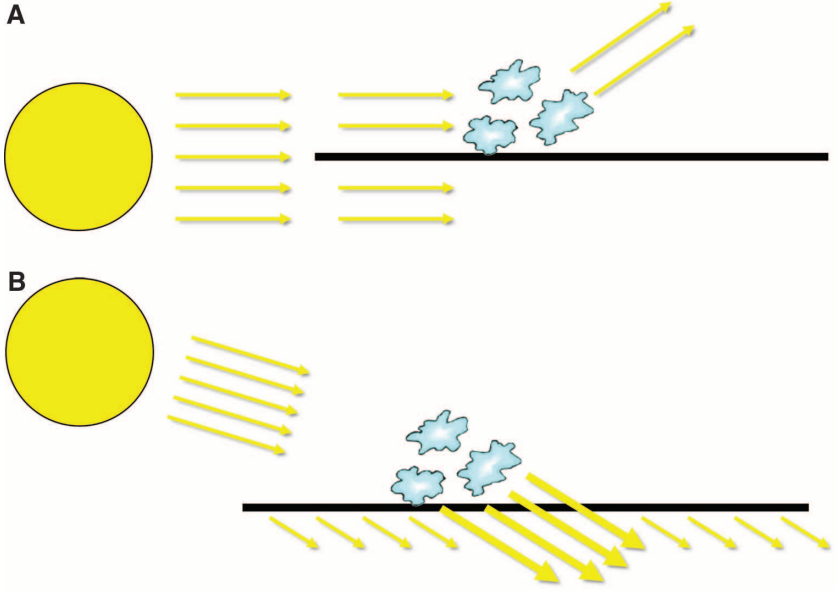

Fig. 2. Viewing geometry makes the clouds visible. (**A**) In this cartoon, sunlight (yellow) approaches the rings (black) nearly edge-on during the equinox event, causing them to appear very dark. However, a cloud of ejecta above the rings (blue) can scatter light toward the camera. (**B**) In this cartoon, sunlight is scattered forward (i.e., at high phase angles) much more efficiently by the dusty ejecta cloud than by the largely dust-free main ring.

was fully illuminated (Fig. 2A). The observed bright streaks (code-named "Ax," "Bx," and "Cx," after the ring region in which each feature was seen, with "x" indicating that it was seen during the equinox event) are measured to be canted (Fig. 3, A and B) by a few degrees from the azimuthal direction. The feature Ax, observed on two occasions, showed a cant angle θ decreasing with time. The most likely reason for an ejecta cloud to evolve in this way is if it was produced quickly (for example, within a fraction of an hour, much less than the orbital periods of between 6 and 14 hours in the rings), with subsequent evolution of each constituent particle on an independent Keplerian orbit. An impact is the most likely way to produce an ejecta cloud so quickly.

We also report here observations of smaller ejecta clouds at nonequinox times in highly forward-scattering geometries (i.e., at phase angle $\alpha > 172°$), in which dust (i.e., micrometer-size) particles brighten considerably as a result of diffraction. Free-floating dust is not abundant in the background ring, as it gets swept into the regoliths of larger particles (*15*), so the dusty ejecta clouds appeared with greatly enhanced contrast in this geometry (Fig. 2B). Cassini images at such high phase angles are only possible when the spacecraft is passing through the planet's shadow, as the safety of its optical instruments would be jeopardized by pointing them so close to the Sun's direction at any other time; furthermore, the small features we report here can only be seen when Cassini is at close range to the rings. These conditions were met for four images in 2005, in which we report five observed ejecta clouds (code-named "C1" through "C5"; fig. S1) that are smeared owing to orbital motion of the features during the image exposure. Furthermore, a sixth ejecta cloud ("C6"; Fig. 1E) was seen in follow-up images in 2012.

The most interesting feature in our data set is Ax, of which two independent observations allow us to investigate the evolution of both its cant angle and its brightness.

Particles with initially identical longitudes on circular orbits with different radial distances will drift apart in longitude because of Keplerian shear, a straightforward consequence of Kepler's third law. Thus, the shape of an initially compact cloud will quickly become dominated by a cant angle θ (Fig. 3B and fig. S5), which is given by (supplementary text 3)

$$\tan\theta = \frac{P}{3\pi t} \qquad (1)$$

where t is the time elapsed and P is the orbital period. This curve is plotted as the solid line in Fig. 3C, where it is seen that the measured cant angles for apparitions Ax(1) and Ax(2) make an excellent fit to the model, implying that Ax was 1.8 orbital periods old (i.e., 23.5 hours) when it was first observed.

We considered the possibility that the observed ejecta clouds were created by the impact of a single solid object with the rings. Because such an impact would throw ejecta in every direction from a single impact point, the cant angle $\theta(t)$ would evolve in a more complex manner due to the noncircularity of ejecta orbits, and we found that this model makes a much poorer fit to the observations (supplementary text 3). The solid impactor model also cannot readily account for the horizontally aligned initial structure of Ax (supplementary text 5) and the volume of observed ejecta (supplementary text 9), so we will assume henceforth that the impacting mass was a broader (but still well-confined) stream of impacting material.

The measured brightness evolution of Ax also supports its identification as an ejecta cloud. Ejecta raised above an orbiting planetary ring does not "land" in the same way as in the more familiar scenario of ejecta raised above a solid surface. Rather, because of Kepler's laws of orbital motion, the ejecta simply pass through the ring once every half-orbit at low relative speeds, and only a fraction equal to $e^{-\tau}$ (where τ is the ring's optical depth) will encounter ring material and be removed from the cloud. The time elapsed between the two observations of Ax corresponds to four half-orbits, regardless of the impactor model discussed above. Thus, we can use the ratio of the two observations of the cloud's total integrated brightness to independently calculate the optical depth of Saturn's A ring (supplementary text 4). Accounting for the different geometries of the two observations, we obtain $\tau \sim 0.65$ for the A ring, in good agreement with other independent measurements of this quantity (*16*) and confirming our interpretation of the observed structures as evolving ejecta clouds.

Several of the observed ejecta clouds, including Ax(1), Bx, and C6, are asymmetric, such that the brightest point is noticeably offset from the apparent center of the cloud (Fig. 1). When the effects of the cant angle are removed, the core structure of Ax(1) is revealed to be azimuthally elongated by a factor of ~7 (fig. S8). We interpret this to constrain the length and width of the impactor stream (supplementary text 5), which we suggest was formed from an interplanetary meteoroid that broke apart as a result of an impact and entered saturnian orbit upon its

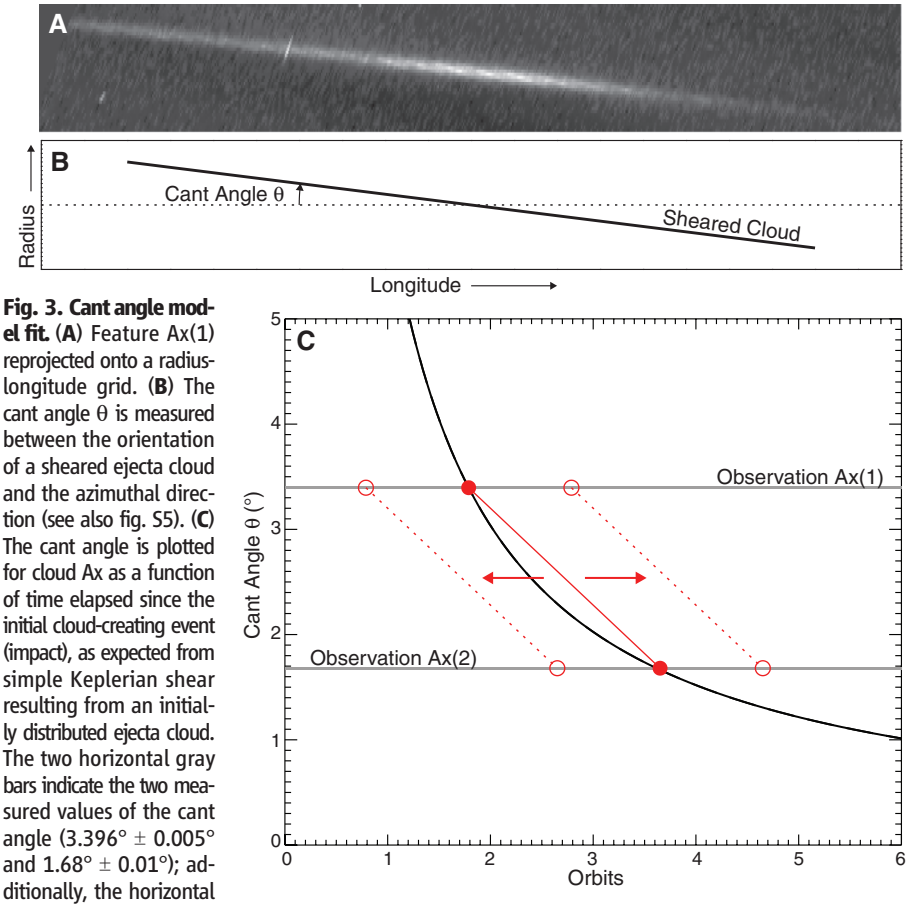

Fig. 3. Cant angle model fit. (**A**) Feature Ax(1) reprojected onto a radius-longitude grid. (**B**) The cant angle θ is measured between the orientation of a sheared ejecta cloud and the azimuthal direction (see also fig. S5). (**C**) The cant angle is plotted for cloud Ax as a function of time elapsed since the initial cloud-creating event (impact), as expected from simple Keplerian shear resulting from an initially distributed ejecta cloud. The two horizontal gray bars indicate the two measured values of the cant angle (3.396° ± 0.005° and 1.68° ± 0.01°); additionally, the horizontal distance between each pair of red circles is fixed by the time elapsed between the two measurements (24.5 hours, or 1.86 orbital periods), so the line connecting each pair has a fixed length and orientation. However, the assemblage can slide horizontally because the time of the initial impact is not directly known (the directions in which the solution can vary are indicated by the red arrows, open circles, and dotted lines). The solid red circles connected by the solid red line indicate where the solid curve passes through the first cant angle measurement, resulting in a residual at the second cant angle measurement of only 0.02°, which is 0.9σ given our estimated measurement error (supplementary text 3).

first encounter with the rings [compare to (*17*)], then produced the observed ejecta cloud upon its second encounter. Keplerian shear would cause the stream to spread along-track to the inferred length in ~8 hours, implying that the impacting material reached an apoapse of ~160,000 km before returning to the ring (supplementary text 5).

The peripheral regions of feature Cx (Fig. 1 and fig. S9) have a steeper cant angle than the bright central region, possibly because the different parts of the cloud have different ages, though it may be that the central region is somehow distended and that the cant angles in the peripheral regions give the feature's true age (supplementary text 6).

Feature C6 was imaged at multiple wavelengths. Its reddish slope (*18*) could be explained by a deficit of particles in the ejecta cloud with radii smaller than $s_{min} \approx 3$ μm (supplementary text 7).

From our measurements of the total integrated brightness of each observed feature (supplementary text 2), the ejecta mass can be estimated (supplementary text 8) if we make an assumption about the particle-size distribution $n(s)$ of the ejecta. For simplicity, we use a power-law model $n(s) = n_0 s^{-q}$, where $n(s)ds$ is the number of particles with radius between s and $s + ds$, though the real particle-size distribution may be more complex. Under this model, we find that the cloud mass is a strong function of q. In particular, when we assume minimum and maximum particle sizes $s_{min} = 3$ μm and $s_{max} = 3$ cm (supplementary text 8), the cloud mass is four orders of magnitude larger for $q < 3$ than it is for $q > 4$ and transitions quickly between the two values for $3 < q < 4$ (fig. S10).

As discussed above, we can estimate the initial ejecta mass by multiplying the mass inferred for the observed cloud by a factor $e^{N\tau}$ (supplementary text 8), where N is the number of half-orbits completed since the cloud formed as inferred from its cant angle, and τ is the optical depth of the ring at the relevant location (*19*). In the absence of detailed calculations of impacts into rings, we then estimate the mass of the impactor by assuming that the ejecta mass is greater than the impacting mass by a yield factor $Y \approx 10^4$ (supplementary text 9). Using the dimensions of each observed feature to estimate the area of the ring affected by impacting material, we find that the available target ring mass is sufficient to account for the observed cloud only if q is not too small and/or s_{max} is not too large (or, equivalently and more generally for the case of non–power-law particle-size distributions, if large ejecta particles are not too abundant). We estimate the Ax impactor to have been between 1 and 10 m in radius before breakup, with the uncertainty mostly due to the particle-size distribution, the assumed yield, and other systematic effects (fig. S11). For the same reason, we estimate the other ejecta clouds reported here to have been due to impactors with radii between 1 cm and 1 m before breakup.

Using the fractional area coverage of the respective ring for each sequence of images that detected a feature described in this work, and taking each observed ejecta cloud's apparent age (table S2) as an estimate of the time for which it remained visible, we estimate the influx of meteoroids to the Saturn system (Fig. 4 and supplementary text 10). This empirical estimate of centimeter-to-meter-size meteoroids in the outer solar system fills a gap between measurements of micrometer-size dust by Pioneer, Ulysses, and New Horizons (*1*, *8*, *20*) and ~10-km objects that are seen directly. To date, little is known about small macroscopic particles in the outer solar system, with most investigators assuming that the Pioneer and Ulysses data justify the extrapolation of measurements in Earth's vicinity.

Our results are higher than the extrapolation by one or two orders of magnitude (Fig. 4); at face value, especially if this increase is also reflected in submillimeter-to-millimeter-size particles, then pollution and erosion rates due to interplanetary meteoroids might be higher than have been thought. However, gravitational focusing enhances the flux at Saturn's rings by a factor of 4 to 40 (*20*, *21*), and the sensitivity of rings to a two-directional flux yields another factor of 2, so our results may corroborate the previous extrapolation after all.

No ejecta clouds were observed in the region dominated by spokes, though we cannot rule out the possibility that spoke-forming impacts may also form ejecta clouds. The intersection between our size distribution and the observed spoke-forming rate (*21*, *22*) indicates that spokes are due to meteoroids of radius ~10 to 50 cm (supplementary text 11).

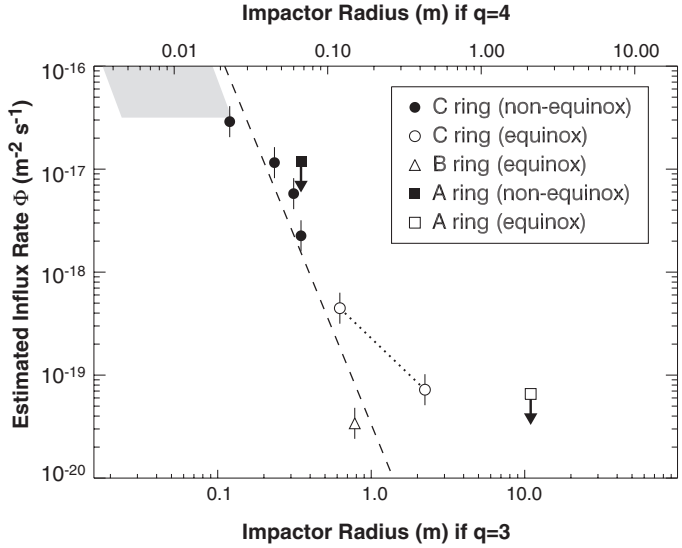

Fig. 4. Impactor size spectrum. Estimated cumulative influx rate of interplanetary meteoroids at 10 astronomical units (AU), not corrected for Saturn's gravitational focusing, as a function of inferred impactor radius (before preliminary breakup). The vertical error bars indicate the Poisson uncertainty in estimating the influx rate from a small number of events. Horizontal uncertainties in the individual data points (e.g., from the measurement of the cloud's brightness) are smaller than the plotted symbols, but systematic uncertainties that may cause all the data points to move horizontally together are quite large. The largest systematic uncertainty is the particle-size distribution (represented by the power-law index q) of the observed clouds, which is indicated by the difference between the upper and lower horizontal axes; other sources of systematic error include the yield factor Y, the albedo ϖ_0, and the phase function $P(\alpha)$ (supplementary texts 2 and 9), which may further move the horizontal axis by as much as a factor of several. The gray region is the micrometeoroid population estimated by scaling the near-Earth population by outer solar system dust measurements (*1*, *8*); its horizontal breadth is the systematic uncertainty due to q. As detailed in supplementary text 10 and figs. S6 and S7, the lowest filled circle is the 2012 detection of C6, whereas the other three filled circles are the 2005 detections of C1 through C5. The filled square with downward-pointing arrow is the nondetection of A-ring objects in the sequence of images that captured C6. The open triangle is equinox feature Bx. The two open circles connected by a dotted line represent the peripheral regions (left) and central region (right) of equinox feature Cx; the peripheral regions (the left-hand circle) may be the more reliable data point (supplementary texts 6 and 9). The open square is Ax, with downward-pointing arrow to indicate that the detection may be coincidental rather than indicative of the influx rate (supplementary text 10). The dashed line is fitted to all the data points that lack arrows. The fitted cumulative number flux of interplanetary meteoroids at 10 AU is $\Phi \approx (3 \times 10^{-9}\ \mathrm{m^{-2}\ s^{-1}})\ R_{impactor}^{-3.6}$ for $q = 3$ and $R_{impactor}$ in meters.

References and Notes

1. J. N. Cuzzi, P. R. Estrada, *Icarus* **132**, 1 (1998).
2. R. H. Durisen, P. W. Bode, J. N. Cuzzi, S. E. Cederbloom, B. W. Murphy, *Icarus* **100**, 364 (1992).
3. S. Charnoz, L. Dones, L. W. Esposito, P. R. Estrada, M. M. Hedman, in *Saturn from Cassini-Huygens*, M. Dougherty, L. Esposito, S. M. Krimigis, Eds. (Springer, Dordrecht, Netherlands, 2009), pp. 537–575.
4. C. K. Goertz, G. Morfill, *Icarus* **53**, 219 (1983).
5. C. Mitchell, C. Porco, L. Dones, J. Spitale, *Icarus* 10.1016/j.icarus.2013.02.011 (2013).

6. M. R. Showalter, *Science* **282**, 1099 (1998).
7. R. S. French *et al.*, *Icarus* **219**, 181 (2012).
8. E. Grün, H. A. Zook, H. Fechtig, R. H. Giese, *Icarus* **62**, 244 (1985).
9. S. Bouley *et al.*, *Icarus* **218**, 115 (2012).
10. L. S. Chambers, J. N. Cuzzi, E. Asphaug, J. Colwell, S. Sugita, *Icarus* **194**, 623 (2008).
11. Some "flashes" of unknown provenance were reportedly seen in Voyager data (*23, 24*), but these have not been confirmed nor generally accepted.
12. C. C. Porco *et al.*, *Space Sci. Rev.* **115**, 363 (2004).
13. Details of our observations and data reduction are given in sections 1 and 2 (respectively) of the supplementary materials text.
14. A. Van Helden, in *Saturn*, T. Gehrels, M. S. Matthews, Eds. (Univ. of Arizona Press, Tucson, AZ, 1984), pp. 23–43.
15. M. S. Tiscareno, in *Planets, Stars, and Stellar Systems, Volume 3: Solar and Stellar Planetary Systems*, T. D. Oswalt, L. French, P. Kalas, Eds. (Springer, Dordrecht, Netherlands, in press); http://arxiv.org/abs/1112.3305.
16. P. D. Nicholson, M. M. Hedman, *Icarus* **206**, 410 (2010).
17. M. M. Hedman, J. A. Burns, M. W. Evans, M. S. Tiscareno, C. C. Porco, *Science* **332**, 708 (2011).
18. All measured brightnesses are relative to the ring background.
19. J. E. Colwell *et al.*, in *Saturn from Cassini-Huygens*, M. Dougherty, L. Esposito, S. M. Krimigis, Eds. (Springer, Dordrecht, Netherlands, 2009), pp. 375–412.
20. A. R. Poppe, M. Horányi, *Geophys. Res. Lett.* **39**, 15104 (2012).
21. J. N. Cuzzi, R. H. Durisen, *Icarus* **84**, 467 (1990).
22. E. Grün, G. W. Garneau, R. J. Terrile, T. V. Johnson, G. E. Morfill, *Adv. Space Res.* **4**, 143 (1984).
23. A. F. Cook, T. C. Duxbury, *J. Geophys. Res.* **86**, 8815 (1981).
24. A. F. Cook, R. Barrey, G. E. Hunt, *Bull. Am. Astron. Soc.* **15**, 814 (1983).

Acknowledgments: We thank M. Showalter for helpful discussions and for the use of Mie scattering code. We thank the Cassini project and the Cassini Imaging Team for making these observations possible. M.S.T. acknowledges funding from the NASA Cassini Data Analysis program (NNX08AQ72G and NNX10AG67G) and the Cassini project. C.D.M. acknowledges funding from the Science and Technology Facilities Council (grant ST/F007566/1).

Supplementary Materials

www.sciencemag.org/cgi/content/full/340/6131/460/DC1
Supplementary Text
Figs. S1 to S11
Tables S1 to S7
References (*25–38*)

3 December 2012; accepted 18 March 2013
10.1126/science.1233524

Melting of Iron at Earth's Inner Core Boundary Based on Fast X-ray Diffraction

S. Anzellini,[1]* A. Dewaele,[1] M. Mezouar,[2] P. Loubeyre,[1] G. Morard[3]

Earth's core is structured in a solid inner core, mainly composed of iron, and a liquid outer core. The temperature at the inner core boundary is expected to be close to the melting point of iron at 330 gigapascal (GPa). Despite intensive experimental and theoretical efforts, there is little consensus on the melting behavior of iron at these extreme pressures and temperatures. We present static laser-heated diamond anvil cell experiments up to 200 GPa using synchrotron-based fast x-ray diffraction as a primary melting diagnostic. When extrapolating to higher pressures, we conclude that the melting temperature of iron at the inner core boundary is 6230 ± 500 kelvin. This estimation favors a high heat flux at the core-mantle boundary with a possible partial melting of the mantle.

Earth's inner core grows by solidification from the surrounding outer core, which is composed of molten iron (Fe) alloyed with ~10 weight percent light elements (*1*). Seismological data reveal important physical properties of the core, such as density (and, hence, pressure) and elasticity; however, they cannot directly reveal the corresponding temperature. Temperature in the core places important constraints on parameters like heat flux to the mantle, power for the geodynamo, and cooling rate, all of which are fundamental to Earth's heat budget and dynamics (*2*).

The temperature at the inner core boundary (ICB) is bracketed between the melting temperature of pure Fe at 330 GPa and the liquidus temperature of the outer core iron-rich alloy (*3*) [expected to be depressed by ~700 K (*4*)]. Neither dynamic (*5–7*) and static (*8–11*) compression measurements nor thermodynamic modeling (*12–15*) have resulted in a consensus on ICB melt-

[1]Commissariat à l'Énergie Atomique, Direction des Applications Militaires Île de France 91297 Arpajon Cedex, France. [2]European Synchrotron Radiation Facility, BP 220, F-38043 Grenoble Cedex, France. [3]Institut de Minéralogie et de Physique des Milieux Condensés UMR CNRS 7590, Université Pierre et Marie Curie, 75005 Paris, France.

*Corresponding author. E-mail: simone.anzellini@cea.fr

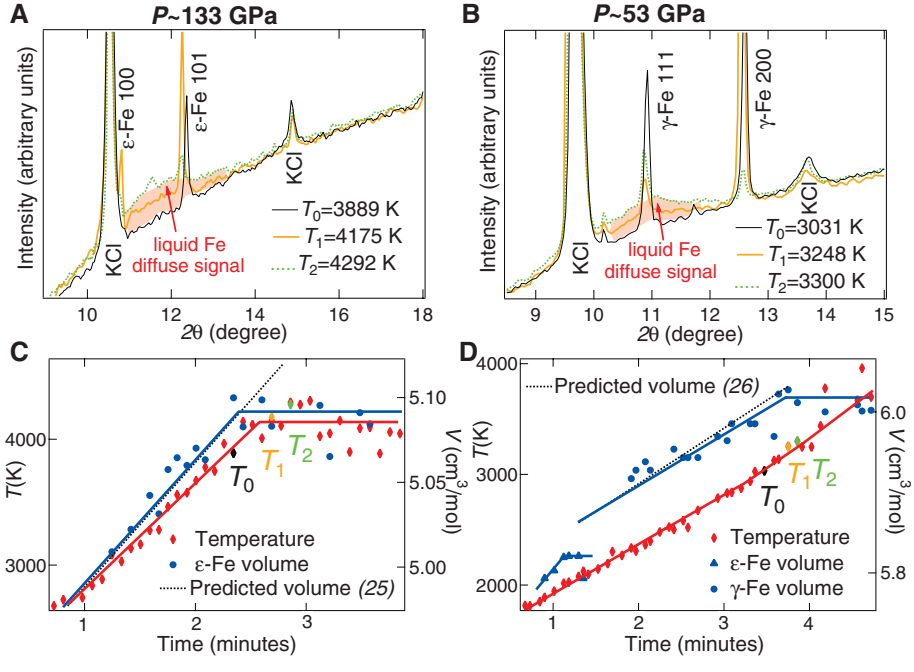

Fig. 1. XRD patterns as a function of temperature, pressure, and time. (**A** and **B**) XRD patterns of a ≈3-μm-thick (≈7-μm-thick) sample during a heating series at $P \approx 133$ GPa and 53 GPa, respectively, recorded at different temperatures. γ-Fe, ε-Fe, and KCl pressure medium diffraction peaks are labeled. Liquid Fe is evidenced by a diffuse ring at $2\theta = 10°$ to 13.5°. (**C** and **D**) Pyrometry temperature, measured and predicted (*25*, *26*). Fe volume as a function of time for the thin (C) and thick (D) samples. The laser's power is linear with time. Data are in table S1.